https://dx.doi.org/10.1016/j.jallcom.2022.163649

Boosting electrochemical performance of Li-S batteries by cerium-based MOFs coated with polypyrrole

Xiaohua Chen[ac], Mi Zhang[b], Jin Zhu[a], Juan Wang[b], Zengbao Jiao[c], Yong Li[b]

a State Key Laboratory for Advanced Metals and Materials, University of Science and Technology Beijing, Beijing 100083, China
b Xi'an Key Laboratory of Clean Energy, Xi'an University of Architecture & Technology, Xi'an, Shanxi 710055, China
c Department of Mechanical Engineering, The Hong Kong Polytechnic University, Hong Kong, China

Abstract

Lithium-sulfur (Li-S) batteries are a promising next-generation energy storage technology due to high theoretical energy density, low cost and abundant reserves. However, the poor electronic conductivity of sulfur and huge volume change hindered their commercial applications. In this paper, selected as a cathode host of Li-S batteries from two Ce-MOFs with dissimilar open metal sites for the first time, Ce-MOF-808 was synthesized and then coated with a Polypyrrole (PPy) layer (Ce-MOF-808@S/PPy). Material characterization and electrochemical performance tests were conducted. Results show that Ce-MOF-808@S/PPy has a high specific surface area of 437.491 m2 g−1, with special micro-mesoporous structures. Ce-MOF-808@S/PPy composite possesses the initial discharge specific capacity of 1612.5 mA h g−1 and discharge specific capacity of 771.9 mA h g−1 at 0.1 C after 100 cycles. Additionally, the battery still maintains a reversible specific capacity above 470 mAh g−1 with 40% capacity retention rate at a rate of 2 C after 200 cycles of charge and discharge. Improved electrochemical performances are mainly attributed to the Ce-MOFs with special micro-mesoporous structures and high specific surface area conducive to inhibiting the shuttle effect and volume expansion through physical adsorption and stable channel structures, the Ce sites with unique adsorption and catalytic effect, and the PPy coating layer adsorbing the polysulfide and acting as charge collectors to enhance conductivity.

Keywords: High-entropy alloys; Precipitation strengthening; Nano-precipitates; Stacking fault; Mechanical properties.

1. Introduction

Recently, Lithium-sulfur (Li-S) batteries have been widely studied for superior theoretical capacity (1675 mA h g^{-1}) and natural abundance of S [1], [2]. However, there are still several drawbacks for Li-S batteries, such as poor rate performance owing to electronic insulation of sulfur and its discharge products (Li_2S/Li_2S_2), the inferior cycle stability for drastic volume expansion, and the rapid capacity decay caused by the dissolution and parasitic shuttle effect of the intermediate lithium polysulfides (Li_2S_n, $4 \leq n \leq 8$) in organic liquid electrolyte [3], [4], [5].

To solve these problems, researchers have proposed strategies to optimize the performance of Li-S batteries. For instance, carbon, metal oxides and metal carbides have been employed as the main host of the element sulfur [6]. In recent decades, metal organic frameworks (MOFs) and their derivatives as the positive electrode body of Li-S batteries have attracted widespread attention. MOF is composed of organic ligands and inorganic metal ions, which is widely used for catalysis, sensing, electrochemistry and separation fields for its high surface area, flexible pore size and the flexibility of structure design [7], [8], [9], [10]. Most previous reports like Chen et al. [11] and others [12], [13], [14], [15] have done some work on the physical effect of MOF and found that pores with adjustable size can separate polysulfides and lithium ions selectively. Regrettably, undesirable electronic conductivity for MOFs was obtained [16], [17], [18], [19]. Hence, it's popular that MOFs composites with conductive supports are employed to boost the conductivity of corresponding materials and the electrochemical performance. There is no doubt that conducting polymer materials like PANi, PEO and PPy have been widely investigated because of their outstanding electrical conductivity [20], [21], [22]. Conductive polymers play an important role in lithium-sulfur batteries [23], [24]. On the one hand, conductive polymers can greatly improve the poor conductivity of sulfur anodes, speed up the transmission of electrons, and improve electrochemical performance. On the other hand, conductive polymers contain polar bonds, such as =C–H, N-H, etc. These polar bonds can chemically anchor polysulfides through bond formation and inhibit the shuttle effect. Therefore, not only conducting polymer materials adsorb the polysulfide, but also they can act as charge collectors to enhance conductivity.

Major MOFs which can only physically prevent polysulfide are still inefficient. Attempts have been made to coat or dope materials (such as metal oxides and so on) that have a catalytic effect on polysulfides [25], [26]. Therefore, an ideal method should be developed to manufacture MOF-based cathode material which possesses catalytic ability and good conductivity. In recent reports, CeO_2 can well adsorb polysulfides and catalyze the conversion of polysulfides thereby improving the electrochemical performance [27]. Ce-MOFs were commonly used in separator materials and other fields [28], [29], [30], [31], [32], [33]. Ce-MOF as the cathode host for Li-S batteries has been seldom reported. In this paper, two types of Ce-MOFs with dissimilar open metal sites, namely Ce-MOF-808 and Ce-UiO-66-BPDC, were synthesized as cathode hosts of Li-S batteries for the first time. PPy layer was coated on the surface of Ce-MOF-808 loaded the sulfur (labeled as Ce-MOF-808@S/PPy). Ce-MOF-808 possesses special micro-mesoporous structures and high surface area, which are conducive to inhibiting the shuttle effect and volume expansion through physical adsorption and stable channel structures. Despite unique adsorption and catalytic effect of Ce, PPy coating layer can improve the intrinsic inferior conductivity. As a result, Ce-MOF-808@S/PPy composite as an active material shows excellent electrochemical performances.

2. Experimental methods

2.1. Materials

Materials used are as follows: Ammonium cerium nitrate ($Ce(NH_4)_2(NO_3)_6$), pyrrole, ethyl alcohol, ammonium persulphate (APS), benzene-1,3,5-tricarboxylic acid (H_3BTC), p-toluene sulfonic acid(p-TSA), electrolyte of 1 M LiTFSI and 1 wt% $LiNO_3$ in DOL/DME (v: v = 1:1), acetylene black (AB), biphenyl-4,4′-dicarboxylic acid, N,N-dimethylformamide (DMF), polyvinylidene fluoride (PVDF), sulfur (S), polyvinyl acetate (PVA) and N-methyl-2-pyrrolidone (NMP). All chemical reagents were purchased from commercial sources without further purification.

2.2. Preparation of Ce-MOF-808, Ce-UiO-66-BPDC

To prepare Ce-MOF-808, 0.28 g benzene-1,3,5- tricarboxylic acid was dissolved in 15 mL DMF under the continuous magnetic stirring. Then the solution mixture was sonicated for 30 min and named as A solution. After this, 2.25 g ammonium cerium nitrate was dissolved in 8 mL deionized water, and then added dropwise to the A solution under the continuous magnetic stirring, followed by heat treatment at 100 °C for 30 min. The final suspension was washed twice with DMF and ethyl alcohol separately, and then dried at 60 °C for 2 h, thereby the target product Ce-MOF-808 was obtained.

To prepare Ce-UiO-66-BPDC, 0.25 g biphenyl-4,4′-dicarboxylic acid was dissolved in 15 mL DMF under the continuous magnetic stirring. Then the solution mixture was sonicated for 30 min and named as B solution. After this, 1.45 g ammonium cerium nitrate was dissolved in 5 mL deionized water, and then added dropwise to the B solution under the continuous magnetic stirring, followed by heat treatment at 100 °C for 30 min. The final suspension was washed twice with DMF and ethyl alcohol separately, and then dried at 60 °C for 2 h, thereby the target product Ce-UiO-66-BPDC was obtained.

2.3. Preparation of Ce-MOF-808@S and Ce-UiO-66-BPDC@S

Sulfur powder and Ce-MOF-808 material (mass ratio of 1: 1) were grinded in an agate mortar for 30 min. Sublimed sulfur was successfully introduced into pores of Ce-MOF-808 through melt diffusion at 155 °C for 12 h. By cooling to room temperature, Ce-MOF-808@S composite was obtained. By adopting the same experimental method, Ce-UiO-66-BPDC@S composite was prepared for comparison.

2.4. Preparation of Ce-MOF-808@S/PPy Composites

2.0 mg prepared Ce-MOF-808@S material was dissolved in 1.0 mL water. Then the above mixture was added to a solution of 8.0 mL water with 0.08 g PVA. After stirring for 30 min, 0.3 g p-TSA and 0.02 mL pyrrole monomers were added to the above mixed solution severally, followed by stirring for 2 h. After that, 1.0 mL APS aqueous solution was added dropwise to the above solution and then stirred for 3 h. Finally, the product was washed three times with water and ethyl alcohol separately, and the final product Ce-MOF-808@S/PPy was collected by centrifugation process.

2.5. Fabrication of electrodes

Fig. 1b schematically shows preparation process for Li-S batteries based on Ce-MOF-808@S/PPy composite cathode. Firstly, the PVDF was dissolved in a certain amount of NMP solution, and at the same time, 50 wt% Ce-MOF-808@S/PPy, 30 wt% AB, and 20 wt% PVDF were weighed to prepare a cathode material. Then Ce-MOF-808@S/PPy and AB were uniformly grinded for 30 min, and then the above mixture was added to the prepared NMP solution in which PVDF was dissolved and kept magnetically stirring for 10 h. After this, applying the mixed slurry to the aluminum foil and then transferred it to vacuum oven dried at 60 °C for 12 h, we obtained a cathode electrode sheet (surface loading ~0.5–1.0 mg cm^{-2}). The cathode electrode sheet and the separator were transferred to a glove box (MBRAUN LABSTAR, $H_2O \leq$ 0.1 ppm, $O_2 \leq 0.1$ ppm) filled with argon using a lithium as an anode electrode. The 50 μL electrolyte consists of 1 M LiTFSI and 1 wt% $LiNO_3$ in DME/DOL (v: v = 1:1).

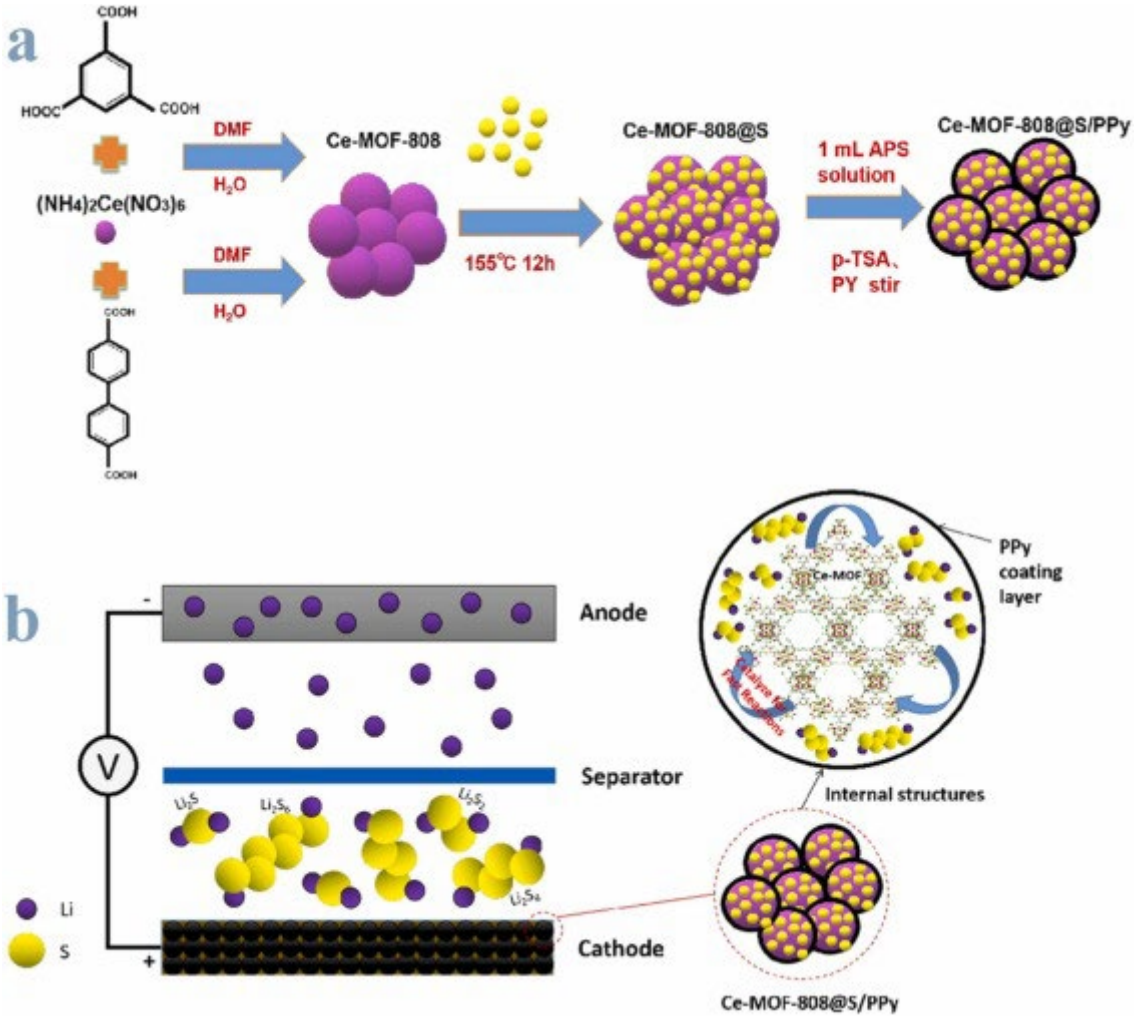

Fig. 1. Schematic diagrams of preparation processes. (a) the Ce-MOF-808@S/PPy composite; (b) Li-S batteries based on Ce-MOF-808@S/PPy composite cathode.

2.6. Materials characterization

Specimens were characterized by a Rigaku D/max2550VB3 + /PC X-ray diffraction (XRD) equipped with Cu Kα rays (λ = 1.5406 Å), at a scan rate of 2° with the range of 0–50°. In order to observe the morphological characteristics and element distribution of materials, scanning electron microscope (SEM) images were taken on a scanning electron microscopy (JEOL 6700F, 5 keV) equipped with an energy-dispersive X-ray spectroscope (EDS, EDX Genesis 4000 X-ray Analysis System). For studying the characteristics of PPy coating layers, transmission electron microscope (TEM) images were taken on a JEM-2010 microscope with an accelerating voltage of 200 kV. To get the specific surface area and pore size distribution, Micromeritics 3-Flex surface-area and pore-size analyzer instrument at 77 K was used for N_2 adsorption measurement. Before testing, all samples were activated under vacuum at 80 °C for 12 h.

2.7. Electrochemical measurements

Cyclic voltammetry (CV) and electrochemical impedance spectroscopy (EIS) tests were conducted by using the PAR2273 electrochemical workstation (Princeton, USA). CV measurement was carried out between 1.3 and 2.9 V at a scan rate of 0.1 mV s^{-1}. EIS was performed under a frequency range of 10^{-2} to 10^{5} Hz with open circuit condition and the amplitude of 5 mV. The battery test system NEWARE-BTS-CT4008–5 V 10 mA (Shenzhen Neware Electronics) was used to carry out the charge and discharge tests at different rates within a voltage range of 1.3–2.9 V vs Li^{+} / Li.

3. Results and discussion

3.1. Characteristics

X-ray diffraction patterns of the sulfur, Ce-MOF-808, Ce-MOF-808@S and Ce-MOF-808@S/PPy composites are shown in Fig. 2. The Ce-MOF-808@S/PPy composite has a stronger diffraction peak intensity than Ce-MOF-808@S [34], [35], [36]. For Ce-MOF-808@S and Ce-MOF-808@S/PPy, the characteristic peaks of the Ce-MOF-808 material have been damaged to a certain extent owing to the heat treatment of the Ce-MOF-808 and sulfur mixture [37], [38], [39].

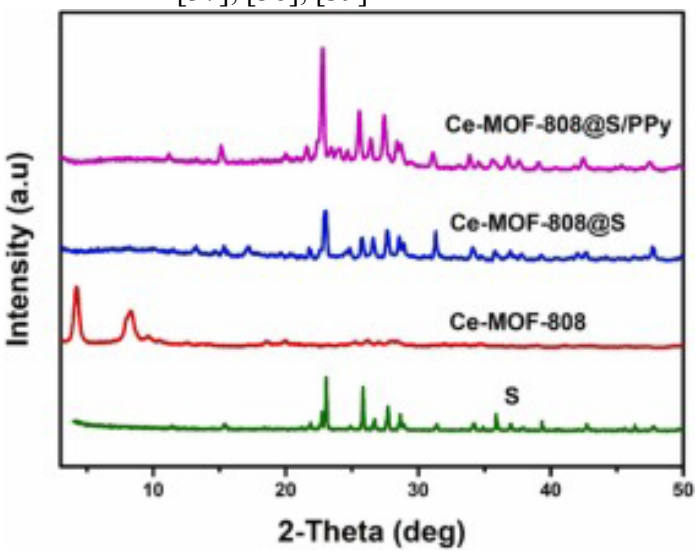

Fig. 2. XRD patterns of S, Ce-MOF-808, Ce-MOF-808@S and Ce-MOF-808@S/PPy composites.

The Fourier transform infrared (FTIR) tests were performed on Ce-MOFs-808 and Ce-MOFs-808@S/PPy respectively. FTIR curves of Ce-MOFs-808 and Ce-MOFs-808@S/PPy are shown in Fig. 3. It can be seen that the characteristic peaks of Ce-MOFs-808 are at 1436 cm^{-1} and 1614 cm^{-1} [20]. In the FITR spectra of Ce-MOFs-808@S/PPy, not only the characteristic peaks of Ce-MOFs-808 are retained, but the characteristic peaks for pyrrole ring, i.e.,1519 cm^{-1}, 1274 cm^{-1} and 1136 cm^{-1} for =C–H, and 1011 cm^{-1} for CN of PPy exist, which proves the recombination of PPy and further shows the successful coating of PPy [21].

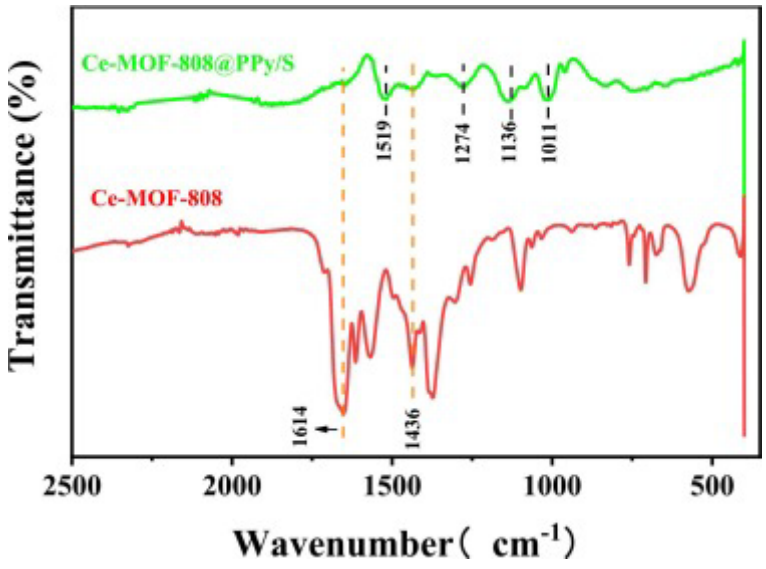

Fig. 3. FTIR curves of Ce-MOFs-808 and Ce-MOFs-808@S/PPy.

SEM morphologies of Ce-UiO-66-BPDC, Ce-MOF-808 are shown in Fig. 4. As exhibited in the Fig. 4a and b, the spherical-like Ce-UiO-66-BPDC was prepared with a size between 200 and 300 nm. Seen from the SEM images of Ce-MOF-808 (Fig. 4c and d), the obtained product is more homogeneous compared to Ce-UiO-66-BPDC.

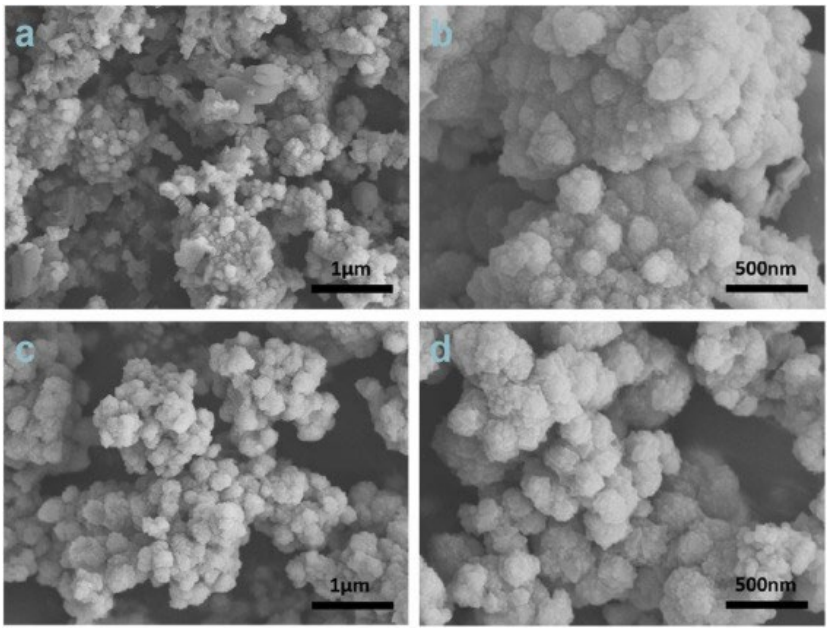

Fig. 4. SEM images. (a, b) Ce-UiO-66-BPDC; (c, d) Ce-MOF-808.

TEM images were characterized to further observe the enlarged morphology and the bonding between PPy and Ce-MOF-808@S. As shown in Fig. 5a and b, Ce-MOF-808 is spherical which is helpful for the transmission of ions, thereby increasing the conductivity and adsorption capacity of the material. The Ce-MOF-808@S is evenly covered with a layer, forming core-shell structure. Effective bonding of Ce-MOF-808@S and PPy increases the contact area between the electrode and the polysulfides generated during the electrode reaction process. The chemical interaction, i.e., formation of Li-N, between PPy and polysulfide was proved to be beneficial to the adsorption of polysulfides in References [20], [22], [40]. Physically and chemically inhibiting the polysulfides into the electrolyte through formation of core-shell structure and Li-N, PPy coating can suppresses the dissolution of polysulfides and reduce loss of the active material, and thus enhance the electrochemical reversibility and cycle stability. Fig. 5c exhibits the elements mapping images of S, C, and Ce respectively, verifying their uniform distribution. The uniform distribution and overlap of the elements S, C and Ce in the EDS mapping images indicate the successful formation of Ce-MOF-808@S/PPy.

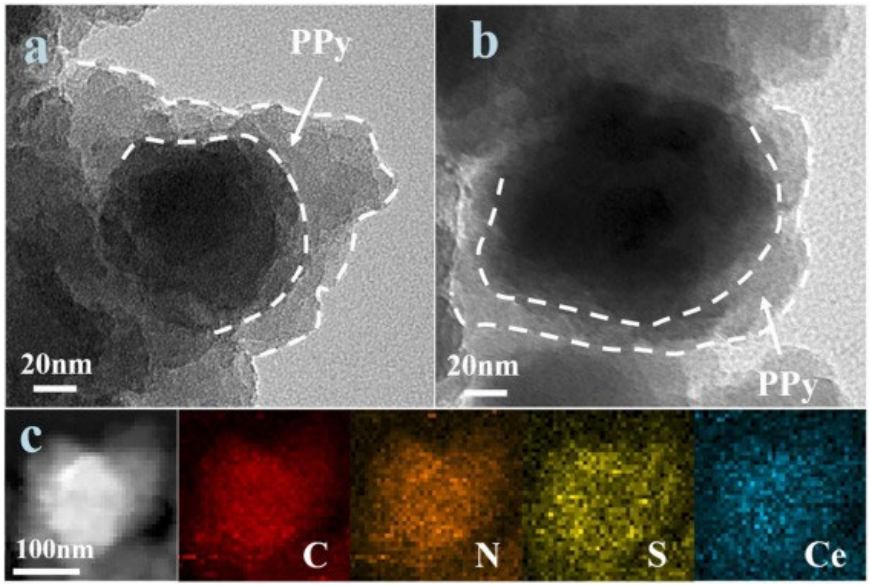

Fig. 5. (a), (b) TEM images of Ce-MOF-808@S/PPy; (c) elemental mapping results of Ce-MOF-808@S/PPy.

N_2 isothermal adsorption-desorption curves of samples Ce-UiO-66-BPDC, Ce-MOF-808 and Ce-MOF-808@S/PPy are shown in Fig. 6a. By pore size analysis (Fig. 6b), there are several micropores (less than 2 nm) and a lot of mesoporous in the Ce-MOF-808 and Ce-MOF-808@S/PPy. By Brunner-Emmet-Teller (BET) measurements, the specific surface areas of the three samples Ce-UiO-66-BPDC, Ce-MOF-808 and Ce-MOF-808@S/PPy are 156.22 $m^2 g^{-1}$, 508.221 $m^2 g^{-1}$, and 437.491 $m^2 g^{-1}$, respectively. The large specific surface area and microporous/mesoporous structure of Ce-MOF-808 and Ce-MOF-808@S/PPy effectively restrict the volume expansion of the cathode material during the electrode reaction process [41], and provide sufficient space to host Li_2S nanoparticles. At the same time, the large specific surface area is also conducive to the contact between the positive electrode and the electrolyte, thereby accelerating

the transmission of lithium ions and improving the electrochemical performance of battery assembled.

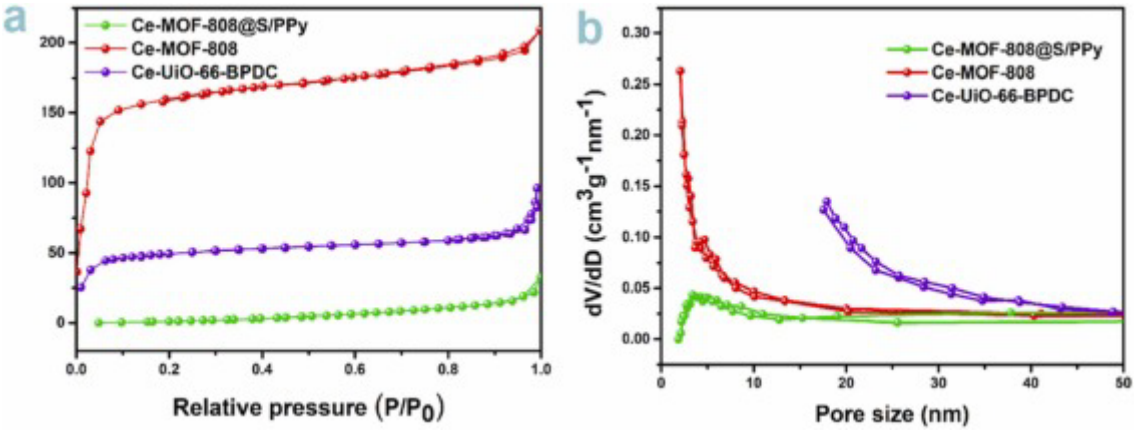

Fig. 6. N_2 isothermal adsorption-desorption curves and pore size distribution curves. (a) N_2 adsorption-desorption isotherms of Ce-UiO-66-BPDC, Ce-MOF-808 and Ce-MOF-808@S/PPy; (b) pore size distribution curves of Ce-UiO-66-BPDC, Ce-MOF-808 and Ce-MOF-808@S/PPy.

3.2. Electrochemical performance

As shown in Fig. 7a, CV curves of Ce-UiO-66-BPDC@S, Ce-MOF-808@S and Ce-MOF-808@S/PPy at the first cycle were measured at 0.1 mV s^{-1} in a voltage range of 1.3–2.9 V (inset of Fig. 7a). CV curves are composed of two reduction peaks and an oxidation peak. Among them, the reduction peak of 2.3 V corresponds to the ring-shaped S_8 reduced long-chain polysulfides, which is the high-voltage discharge platform potential of the lithium-sulfur battery. As a low-voltage discharge platform potential, the peak of 2.0 V corresponds to long-chain polysulfide, which is further reduced to short-chain polysulfide and converted to Li_2S_2 and Li_2S [42], [43], [44], [45]. Fig. 7b shows the CV curves of Ce-MOF-808@S/PPy cathode at 1st, 2nd and 3rd cycles. Both the positive shift of cathodic peaks and the negative shift of anodic peaks after the first cycle of the CV curve indicate that the cell polarization is weakened after the first cycle [38], [39].

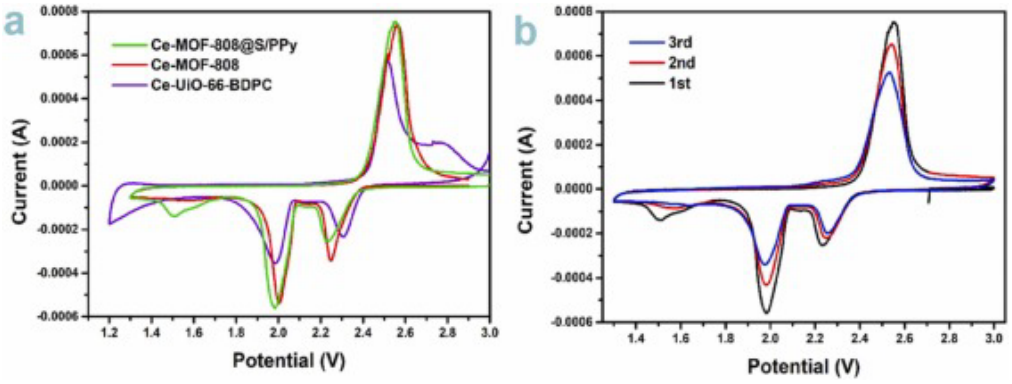

Fig. 7. CV curves. (a) Ce-UiO-66-BPDC@S, Ce-MOF-808@S and Ce-MOF-808@S/PPy electrodes at the first cycle; (b) Ce-MOF-808@S/PPy electrode at 1st, 2nd and 3rd cycles.

Fig. 8a shows Ce-MOF-808@S/PPy charge-discharge curves with different number of cycles at 0.1 C. Flat low-voltage platform near 2.0 V corresponds to the reduction of polysulfides to Li_2S and Li_2S_2 during the electrode reaction. Fig. 8b shows the cycling stability of Ce-UiO-66-BPDC, Ce-MOF-808 and Ce-MOF-808@S/PPy at 0.1 C after loading sulfur and corresponding coulomb efficiency. After 100 cycles at 0.1 C, the Ce-MOF-808@S/PPy, Ce-MOF-808 and Ce-UiO-66-BPDC possess the capacity retention ratios of 57.1%, 33.3%, 25.8%, respectively. The initial discharge specific capacities of Ce-UiO-66-BPDC, Ce-MOF-808 and Ce-MOF-808@S/PPy at 0.1 C are 757 mA h g^{-1}, 910 mA h g^{-1} and 1612.5 mA h g^{-1} respectively. Obviously, the initial discharge specific capacity of Ce-MOF-808@S/PPy is significantly increased by about 70%. Fig. 8c presents the cycle performance of Ce-MOF-808@S/PPy material at 2 C. After 200 cycles, the discharge specific capacity of Ce-MOF-808@S/PPy is still maintained at 470 mAh g^{-1} with 40% capacity retention rate.

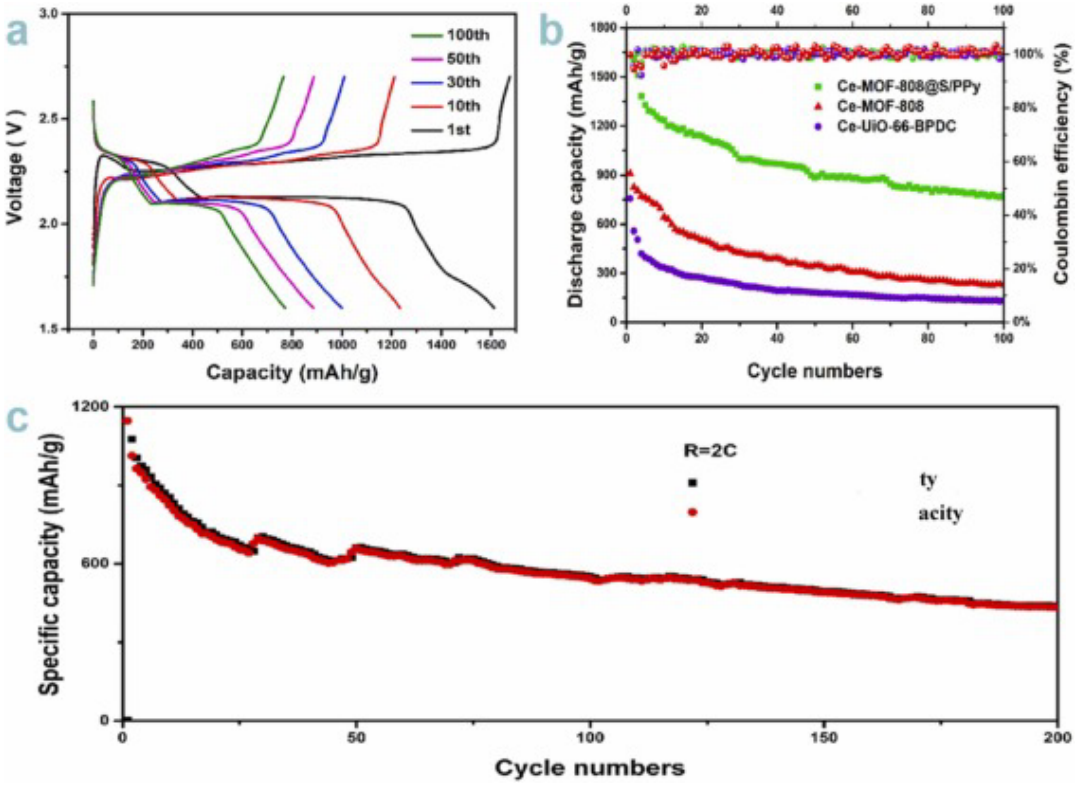

Fig. 8. Electrochemical characterization of Ce-UiO-66-BPDC, Ce-MOF-808, and Ce-MOF-808@S/PPy electrodes after loading sulfur. (a) Ce-MOF-808@S/PPy charge-discharge curves with different number of cycles at 0.1 C; (b) cycle performance at 0.1 C; (c) cycle performance of Ce-MOF-808@S/PPy electrodes at 2 C.

Fig. 9a and b show rate capacities at various C-rates of 0.1 C, 0.5 C, 1 C, and 2 C. For Ce-UiO-66-BPDC the discharge specific capacities are 720, 340, 300, and 240 mA h g^{-1}, respectively, and for Ce-MOF-808, are 1000, 650, 520, and 400 mA h g^{-1}, respectively. For Ce-MOF-808@S/PPy they have reached 1600, 850, 720, and 600 mA h g^{-1}, respectively. By comparing the cycle stability all composites have a great increase in the initial discharge specific capacity, and it decays quickly at a rate of 0.1 C.

As the discharge rate increases, the discharge capacity decay of the material gradually decreases and stabilizes. During the whole cycles, the discharge specific capacities of Ce-MOF-808@S/PPy are always higher than those of Ce-UiO-66-BPDC and Ce-MOF-808 samples. Compared with Ce-UiO-66-BPDC and Ce-MOF-808, Ce-MOF-808@S/PPy has better cycle stability and higher retention ability. It is our common understanding that PPy coating can increase the conductivity of the materials, so when the Ce-MOF-808@S/PPy composite is used as a positive electrode material, the transmission channels relative to Li^+ will be more diversified, which will significantly boost the conductivity of electrode materials. The stable pore structure and large specific surface area of the Ce-MOF-808 can adsorb much polysulfide and alleviate the volume change in the process of charging and discharging, to reduce the dissolution of polysulfides and avoid the "shuttle effect". Moreover, Ce-MOF-808@S/PPy cathode materials can promote the transition of polysulfides from long chain to the short chain, to ensure the penetration of electrolyte and enlarge electrolyte/cathode contact area [45], [46]. In addition, Ce-MOF exhibits unique adsorption and catalyze effect for the existence of Ce sites, which vastly guarantees the sufficient sulfur loading sites [41], [47].

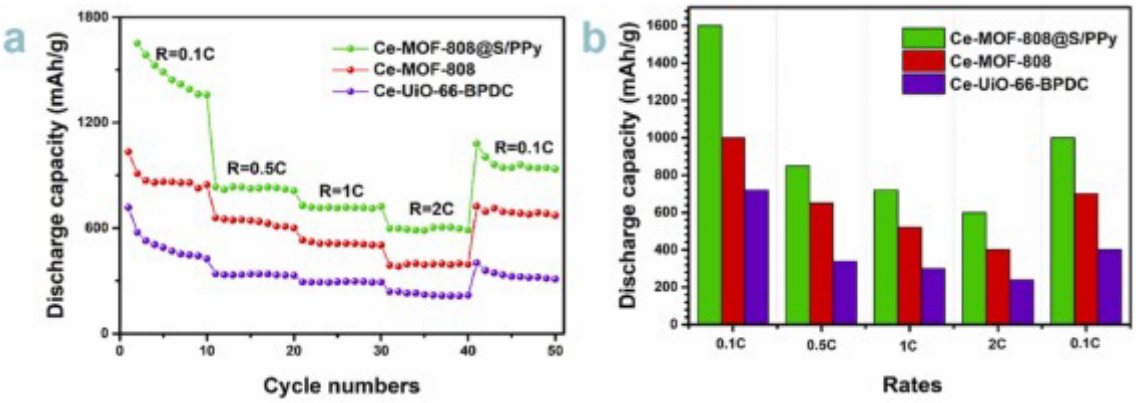

Fig. 9. (a) Rate performance for Ce-UiO-66-BPDC, Ce-MOF-808 and Ce-MOF-808@S/PPy cathode at various C-rate of 0.1 C, 0.5 C, 1 C, and 2 C; (b) histogram comparison of discharge capacities at different C-rates.

Influence of PPy coating layer on the electrode/electrolyte interface was analyzed. EIS measurement, as a reliable electrochemical technique to evaluate transport kinetics, was implemented. Fig. 10 shows EIS curves of Ce-MOF-808 and Ce-MOF-808@S/PPy electrodes. Plots of Z_{real} on the reciprocal root square of the low-frequencies ($\omega^{-1/2}$) for Ce-MOF-808 and Ce-MOF-808@S/PPy electrodes are shown in Fig. 11. Combined with EIS and Zview software analysis, the ohmic resistance (R_s) and charge transfer resistance (R_{ct}) are listed in Table 1. It is clearly seen that Ce-MOF-808@S/PPy shows a minimum R_s, which indicates a thinner solid electrolyte interface. Meanwhile, the R_{ct} of Ce-MOF-808@S/PPy is also minimal, demonstrating more electro-activities generated after PPy coating. Li^+ diffusion coefficient (D) (Table 1) is evaluated by the following formula:(1)D=R2T22A2n2F4C2σ2Where R is gas constant, T is the absolute temperature, F is Faraday constant, A is the surface area of the electrode, n is the number of electrons during the process of Li^+ transportation, C is the

concentration of Li in the lattice, and σ is the Warburg factor and can be obtained from the fitted curve of $Z' \sim \omega^{-1/2}$ (Fig. 11). The D values of Ce-MOF-808 and Ce-MOF-808@S/PPy are fitted to be 7.24×10^{-18} and 1.86×10^{-17} cm^2 s^{-1}, respectively. The Li^+ diffusion coefficient of Ce-MOF-808@S/PPy is 2.5 times that of pure Ce-MOF-808@S, which further confirms that the PPy coating layer effectively facilitates Li^+ transport kinetics of host material.

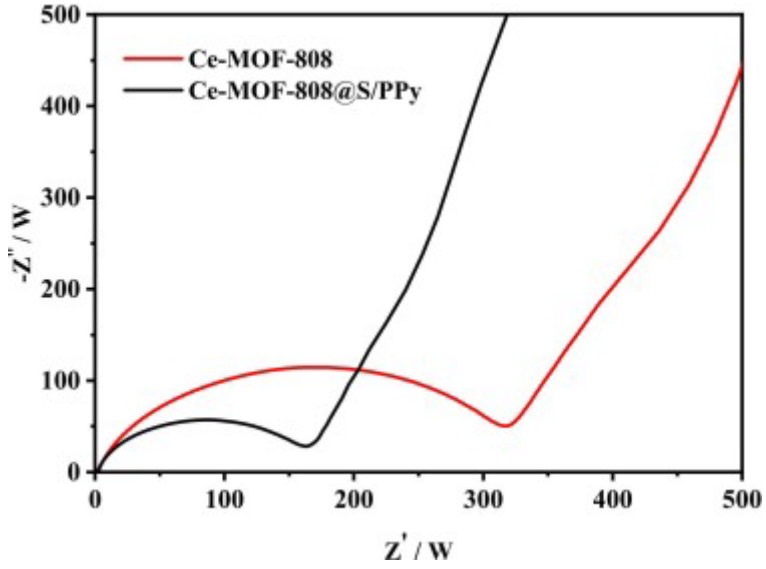

Fig. 10. EIS curves of Ce-MOF-808 and Ce-MOF-808@S/PPy electrodes.

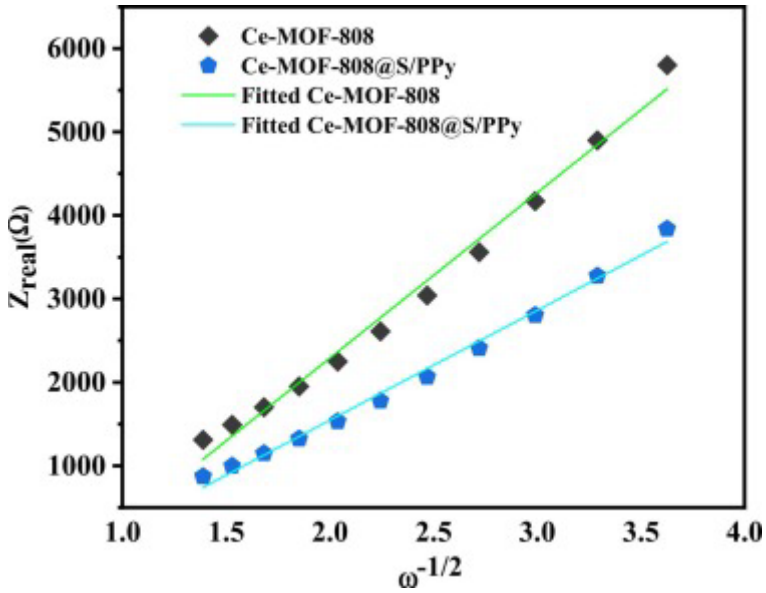

Fig. 11. Plots of Z_{real} on the reciprocal root square of the low-frequencies ($\omega^{-1/2}$) for Ce-MOF-808 and Ce-MOF-808@S/PPy electrodes.

Fig. 12 presents EIS curves of Ce-MOF-808@S/PPy electrode in different cycles. The charge transfer resistance in the first cycle is the largest. It is more stable after cycles. The transfer rate of lithium ions and electrons is improved, which indicates that PPy coating increases the conductivity of materials. By using method of first loading sulfur

and then coating, the shuttle effect can be effectively suppressed, thereby improving the cycle stability of the batteries [21]. After the first cycle, the resistance of the electrodes decreases significantly, which indicates that the interface properties and charge transfer have changed. The decrease in impedance may be caused by the chemical bonds between cerium and sulfur clusters, and the rearrangement of active materials occupies a more favorable position electrochemically, which would lead to the close contact and greater coverage [48]. Then in the subsequent cycles, the impedance spectrum of the Ce-MOF-808@S/PPy electrode would change little and almost stabilize.

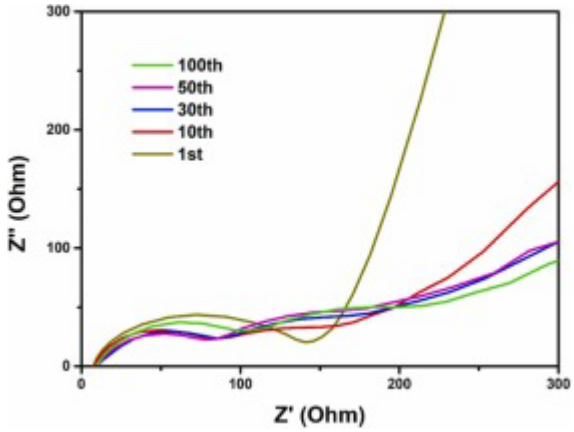

Fig. 12. EIS curves of Ce-MOF-808@S/PPy electrodes in Li-S batteries in different cycles.

4. Conclusion

In conclusion, commonly used in separator materials of batteries, Ce-MOF-808 was used as a cathode host of the Li-S battery for the first time. Ce-MOF-808@S/PPy composite was successfully synthesized with special pore structures, large surface area, stable charge transfer resistance, and Ce sites with catalytic functions. When used as a cathode material for the Li-S battery, it can effectively inhibit the volume expansion and shuttle effect of the battery and make the Li-S battery have a conspicuous electrochemical performance. Ce-MOF-808@S/PPy material cathode possesses the initial discharge specific capacity of 1612.5 mA h g^{-1} and discharge specific capacity of 771.9 mA h g^{-1} at 0.1 C after 100 cycles. The discharge specific capacity for Ce-MOF-808@S/PPy is still maintained at 470 mA h g^{-1} at 2 C after 200 cycles. This work provides a feasible idea for exploring high-performance Li-S batteries based on MOF composites.

Declaration of Competing Interest

The authors declare that they have no known competing financial interests or personal relationships that could have appeared to influence the work reported in this paper.

Acknowledgments

The authors deeply appreciate the fellows Guodong Han, Jia Yao, Jing Zhang, and Xin Wang for providing experimental assistance and meaningful discussion.

References

[1] Y. Pan, Y. Zhou, Q. Zhao, Y. Dou, S. Chou, F. Cheng, J. Chen, H.K. Liu, L. Jiang, S.X. Dou, Introducing ion-transport-regulating nanochannels to lithium-sulfur batteries, Nano Energy 33 (2017) 205–212, https://doi.org/10.1016/j.nanoen.
2017.01.025

[2] Z. Chen, H. Pan, H. Zhong, Z. Xiao, X. Li, R. Wang, Porous organic polymers for polysulfide trapping in lithium-sulfur batteries, Adv. Funct. Mater. 28 (2018) 1707597, https://doi.org/10.1002/adfm.201707597

[3] L. Zhang, M. Ling, J. Feng, L. Mai, G. Liu, J. Guo, The synergetic interaction between LiNO3 and lithium polysulfides for suppressing shuttle effect of lithium-sulfur batteries, Energy Storage Mater. 11 (2018) 24–29, https://doi.org/10.1016/j.
ensm.2017.09.001

[4] S. Deng, Y. Yan, L. Wei, T. Li, X. Su, X. Yang, Z. Li, M. Wu, Amorphous Al2O3 with N-Doped porous carbon as efficient polysulfide barrier in Li–S batteries, ACS Appl.
Energ. Mater. 2 (2019) 1266–1273, https://doi.org/10.1021/acsaem.8b01815

[5] Y.J. Hong, K.C. Roh, Y.C. Kang, Superior lithium-ion storage performances of carbonaceous microspheres with high electrical conductivity and uniform

[6] H.S. Kang, Y.K. Sun, Freestanding bilayer carbon–sulfur cathode with function of entrapping polysulfide for high performance Li–S batteries, Adv. Funct. Mater. 26 (2016) 1225–1232, https://doi.org/10.1002/adfm.201504262

[7] X. Li, X. Yang, H. Xue, H. Pang, Q. Xu, Metal–organic frameworks as a platform for clean energy applications, Energy Chem. 2 (2020) 100027, https://doi.org/10.
1016/j.enchem.2020.100027

[8] M. Du, Q. Li, G. Zhang, F. Wang, H. Pang, Metal–organic framework-based sulfur-loaded materials, Energy Environ. Mater. 0 (2021) 1–16, https://doi.org/10.1002/
eem2.12170

[9] W. Li, X. Guo, P. Geng, M. Du, Q. Jing, X. Chen, G. Zhang, H. Li, Q. Xu, P. Braunstein, H. Pang, Rational design and general synthesis of multimetallic metal–organic framework nano-octahedra for enhanced Li–S battery, Adv. Mater. 33 (2021) 2105163, https://doi.org/10.1002/adma.202105163

[10] P. Geng, M. Du, X. Guo, H. Pang, Z. Tian, P. Braunstein, Q. Xu, Bimetallic metal-organic framework with high-adsorption capacity toward lithium polysulfides for lithium–sulfur batteries, Energy Environ. Mater. (2021) 1–9, https://doi.org/
10.1002/eem2.12196

[11] H. Chen, Y. Xiao, C. Chen, J. Yang, C. Gao, Y. Chen, J. Wu, Y. Shen, W. Zhang, S. Li, Conductive MOF-modified separator for mitigating the shuttle effect of li-thium–sulfur battery through a filtration method, ACS Appl. Mater. Interfaces 11 (2019) 11459–11465, https://doi.org/10.1021/acsami.8b22564

[12] W.W. Jin, J.Z. Zou, S.Z. Zeng, S. Inguva, G.Z. Xu, X.H. Li, M. Peng, X.R. Zeng, Tailoring the structure of clew-like carbon skeleton with 2D Co-MOF for advanced Li-S cells, Appl. Surf. Sci. 469 (2019) 404–413, https://doi.org/10.1016/j.
apsusc.2018.11.052

[13] Y. Lu, X. Gao, Y. Dong, T. Wang, H.L. Chen, H. Maob, Y. Zhao, H. Jiang, Z. Cao,

T. Li, Preparing bulk ultrafine-microstructure high-entropy alloys via direct solidification, Nanoscale 10 (2018) 1912–1919, https://doi.org/10.1039/C7NR07281C
[14] X.F. Liu, X.Q. Guo, R. Wang, Q.C. Liu, Z.J. Li, S.Q. Zang, T.C. Mak, Manganese cluster-based MOF as efficient polysulfide-trapping platform for high-performance lithium–sulfur batteries, J. Mater. Chem. A 7 (2019) 2838–2844, https://doi.org/10.1039/C8TA09973A
[15] P.M. Shanthi, P.J. Hanumantha, B. Gattu, M. Sweeney, M.K. Datta, P.N. Kumta, Understanding the origin of irreversible capacity loss in non-carbonized carbonate-based metal organic framework (MOF) sulfur hosts for lithium-sulfur battery, Electrochim. Acta 229 (2017) 208–218, https://doi.org/10.1016/j.electacta.2017.01.115
[16] X.C. Xie, K.J. Huang, X. Wu, Metal-organic framework derived hollow materials for electrochemical energy storage, J. Mater. Chem. A 6 (2018) 6754–6771, https://doi.org/10.1039/C8TA00612A
[17] Z. Wang, W. He, X. Zhang, Y. Yue, J. Liu, C. Zhang, L. Fang, Multilevel structures of Li3V2 (PO4)3/phosphorus-doped carbon nanocomposites derived from hybrid V-MOFs for long-life and cheap lithium ion battery cathodes, J. Power Sources 366 (2017) 9–17, https://doi.org/10.1016/j.jpowsour.2017.08.078
[18] Z. Li, C. Li, X. Ge, J. Ma, Z. Zhang, Q. Li, C. Wang, L. Yin, Reduced graphene oxide wrapped MOFs-derived cobalt-doped porous carbon polyhedrons as sulfur immobilizers as cathodes for high performance lithium sulfur batteries, Nano Energy 23 (2016) 15–26, https://doi.org/10.1016/j.nanoen.2016.02.049
[19] C. Zhang, J. Dai, P. Zhang, S. Zhang, H. Zhang, Y. Shen, A. Xie, Porous Fe2O3/ZnO composite derived from MOFs as an anode material for lithium ion batteries,
Ceram. Int. 42 (2016) 1044–1049, https://doi.org/10.1016/j.ceramint.2015.09.028
[20] L. Gao, N. Huang, J. Wang, H. Ren, S.W. Joo, J. Huang, Fabrication of polypyrrole coated cobalt manganate porous nanocubes by a facile template precipitation and annealing method for lithium–sulfur batteries, J. Alloy. Compd. 885 (2021) 161350, https://doi.org/10.1016/j.jallcom.2021.161350
[21] H. Jiang, X.C. Liu, Y. Wu, Y. Shu, X. Gong, F.S. Ke, H. Deng, Metal-organic frameworks for high charge-discharge rates in lithium-sulfur batteries, Angew. Chem. Int. Ed. 57 (2018) 3916–3921, https://doi.org/10.1002/ange.201712872
[22] M. Du, X. Wang, P. Geng, Q. Li, Y. Gu, Y. An, H. Pang, Polypyrrole-enveloped Prussian blue nanocubes with multi-metal synergistic adsorption toward lithium polysulfides: high-performance lithium-sulfur batteries, Chem. Eng. J. 420 (2021) 130510, https://doi.org/10.1016/j.cej.2021.130518
[23] H. Gao, S. Ning, Y. Zhou, S. Men, X. Kang, Polyacrylonitrile-induced formation of core-shell carbon nanocages: Enhanced redox kinetics towards polysulfides by confined catalysis in Li-S batteries, Chem. Eng. J. 408 (2020) 127323, https://doi.org/10.1016/j.cej.2020.127323
[24] J. Wu, Y. Dai, Z. Pan, D. Huo, T. Wang, H. Zhang, J. Hu, S. Yan, Co3O4 hollow microspheres on polypyrrole nanotubes network enabling long-term cyclability sulfur cathode, Appl. Surf. Sci. 510 (2020) 145529, https://doi.org/10.1016/j.

apsusc.2020.145529
[25] G. Fang, J. Zhou, C. Liang, A. Pan, C. Zhang, Y. Tang, X. Tan, J. Liu, S. Liang, MOFs nanosheets derived porous metal oxide-coated three-dimensional substrates for lithium-ion battery applications, Nano Energy 26 (2016) 57–65, https://doi.org/10.1016/j.nanoen.2016.05.009
[26] L. Wang, L. Zhao, K. Lan, Progress in porous metal oxide catalysts derived from MOFs, Chemistry 80 (2017) 611–620, https://doi.org/10.14159/j.cnki.0441-3776.2017.07.001
[27] X.J. Hong, C.L. Song, Y. Yang, H.C. Tan, G.H. Li, Y.P. Cai, H. Wang, Cerium based metal-organic frameworks as an efficient separator coating catalyzing the conversion of polysulfides for high performance lithium-sulfur batteries, ACS Nano 13 (2019) 1923–1931, https://doi.org/10.1021/acsnano.8b08155
[28] M. Lammert, M.T. Wharmby, S. Smolders, B. Bueken, A. Lieb, K.A. Lomachenko, D. De Vos, N. Stock, Cerium-based metal organic frameworks with UiO-66 architecture: synthesis, properties and redox catalytic activity, Chem. Commun. 51 (2015) 12578–12581, https://doi.org/10.1039/C5CC02606G
[29] X. Chen, E. Yu, S. Cai, H. Jia, J. Chen, P. Liang, In situ pyrolysis of Ce-MOF to prepare CeO2 catalyst with obviously improved catalytic performance for toluene combustion, Chem. Eng. J. 344 (2018) 469–479, https://doi.org/10.1016/j.cej.2018.03.091
[30] H. Yu, J. Han, S. An, G. Xie, S. Chen, Ce (III, IV)-MOF electrocatalyst as signal-amplifying tag for sensitive electrochemical aptasensing, Biosens. Bioelectron. 109 (2018) 63–69, https://doi.org/10.1016/j.bios.2018.03.005
[31] M. Lammert, C. Glißmann, H. Reinsch, N. Stock, Synthesis and characterization of new Ce (IV)-MOFs exhibiting various framework topologies, Cryst. Growth Des. 17 (2017) 1125–1131, https://doi.org/10.1021/acs.cgd.6b01512
[32] C. Zhu, T. Ding, W. Gao, K. Ma, Y. Tian, X. Li, CuO/CeO2 catalysts synthesized from Ce-UiO-66 metal-organic framework for preferential CO oxidation, Int. J. Hydrogen Energy 42 (2017) 17457–17465, https://doi.org/10.1016/j.ijhydene.2017.02.088
[33] Y. Li, Y. Zhao, X. Feng, X. Wang, Q. Shi, J. Wang, J. Wang, J. Zhang, Y. Hou, A durable P2-type layered oxide cathode with superior low-temperature performance for sodium-ion batteries, Sci. China Mater. (2021), https://doi.org/10.1007/s40843-021-1742-8
[34] J. Shao, H. Zhou, M. Zhu, J. Feng, A. Yuan, Facile synthesis of metal-organic framework-derived Co3O4 with different morphologies coated graphene foam as integrated anodes for lithium-ion batteries, J. Alloy. Compd. 768 (2018) 1049–1057, https://doi.org/10.1016/j.jallcom.2018.07.290
[35] Z. Wang, B. Wang, Y. Yang, Y. Cui, Z. Wang, B. Chen, G. Qian, Mixed-metal-organic framework with effective Lewis acidic sites for sulfur confinement in high-performance lithium–sulfur batteries, ACS Appl. Mater. Interfaces 7 (2015) 20999–21004, https://doi.org/10.1021/acsami.5b07024
[36] N. Yan, W. Zhang, J. Shi, Y. Liu, H. Cui, Nano potassium phosphotungstate spheres/sulfur composites as cathode for Li-S batteries, Mater. Lett. 229 (2018)

198–201, https://doi.org/10.1016/j.matlet.2018.07.007
[37] T. Liu, C. Dai, M. Jia, D. Liu, S. Bao, J. Jiang, M. Xu, C.M. Li, Selenium embedded in metal–organic framework derived hollow hierarchical porous carbon spheres for advanced lithium–selenium batteries, ACS Appl. Mater. Interfaces 8 (2016) 16063–16070, https://doi.org/10.1021/acsami.6b04060
[38] L. Bai, D. Chao, P. Xing, L.J. Tou, Z. Chen, A. Jana, Z.X. Shen, Y. Zhao, Refined sulfur nanoparticles immobilized in metal–organic polyhedron as stable cathodes for Li–S battery, ACS Appl. Mater. Interfaces 8 (2016) 14328–14333, https://doi.org/10.1021/acsami.6b04697
[39] Z. Wang, X. Li, Y. Cui, Y. Yang, H. Pan, Z. Wang, C. Wu, B. Chen, G. Qian, A metal–organic framework with open metal sites for enhanced confinement of sulfur and lithium–sulfur battery of long cycling life, Cryst. Growth Des. 13 (2013) 5116–5120, https://doi.org/10.1021/cg401304x
[40] T. Wu, G. Sun, W. Lu, L. Zhao, A. Mauger, C.M. Julien, L. Sun, H. Xie, J. Liu, A polypyrrole/black-TiO2/S double-shelled composite fixing polysulfides for lithium-sulfur batteries, Electrochim. Acta 353 (2020).
[41] J. He, Y. Chen, W. Lv, K. Wen, C. Xu, W. Zhang, Y. Li, W. Qin, W. He, From metal–organic framework to Li2S@ C–Co–N nanoporous architecture: a high-capacity cathode for lithium–sulfur batteries, ACS Nano 10 (2016) 10981–10987, https://doi.org/10.1021/acsnano.6b05696
[42] M. Zhang, Q. Dai, H. Zheng, M. Chen, L. Dai, Novel MOF-derived Co@ N-C bifunctional catalysts for highly efficient Zn–Air batteries and water splitting, Adv. Mater. 30 (2018) 1705431, https://doi.org/10.1002/adma.201705431
[43] N. Zhang, B. Li, S. Li, S. Yang, Mesoporous hybrid electrolyte for simultaneously inhibiting lithium dendrites and polysulfide shuttle in Li–S Batteries, Adv. Energy Mater. 8 (2018) 1703124, https://doi.org/10.1002/aenm.201703124
[44] L. Li, L. Chen, S. Mukherjee, J. Gao, H. Sun, Z. Liu, X. Ma, T. Gupta, C.V. Singh, W. Ren, Phosphorene as a polysulfide immobilizer and catalyst in high-performance lithium–sulfur batteries, Adv. Mater. 29 (2017) 1602734, https://doi.org/10.1002/adma.201602734
[45] M.E. Zhong, J. Sun, J. Guan, Sulfuric acid-adjuvant sulfonated graphene as efficient polysulfides tamer for high-energy-density Li-S batteries, J. Power Sources 412 (2019) 134–141, https://doi.org/10.1016/j.jpowsour.2018.11.045
[46] H. Liu, W. Pei, W.H. Lai, Electrocatalyzing S cathodes via multisulfiphilic sites for superior room-temperature sodium–sulfur batteries, ACS Nano 14 (2020) 7259–7268, https://doi.org/10.1021/acsnano.0c02488
[47] W. Li, K. Chen, Q. Xu, X. Li, Q. Zhang, J. Weng, J. Xu, Mo2C/C Hierarchical double-shelled hollow spheres as sulfur host for advanced Li-S batteries, Angew. Chem. Int. Ed. 60 (2021) 21512–21520, https://doi.org/10.1002/anie.202108343
[48] J. Gómez-Urbano, J. Gómez-Cámer, C. Botas, N. Díez, J.L. del Amo, L. Rodríguez-Martinez, D. Carriazo, T. Rojo, Hydrothermally reduced graphene oxide for the effective wrapping of sulfur particles showing long term stability as electrodes for Li-S batteries, Carbon 139 (2018) 226–233, https://doi.org/10.1016/j.carbon.2018.06.053